

The non-thermal secondary CMB anisotropies from radio galaxy lobes

Sandeep Kumar Acharya¹*, Subhabrata Majumdar²† and Biman B. Nath³‡

¹*Jodrell Bank Centre for Astrophysics, School of Physics and Astronomy, The University of Manchester, Manchester M13 9PL, U.K.*

²*Department of Theoretical Physics, Tata Institute of Fundamental Research, Mumbai 400005, India*

³*Raman Research Institute, Sadashiva Nagar, Bangalore 560080, India*

Accepted 2021 –. Received 2021 –

ABSTRACT

Current and upcoming high angular resolution and multi-frequency experiments are well poised to explore the rich landscape of secondary CMB anisotropies. In this context, we compute for the first time, the power spectrum of CMB fluctuations from plasma in a cosmological distribution of evolving lobes of giant radio galaxies. We, also, explicitly take into account the non-thermal electron distribution, as opposed to thermal distribution, which has important implications for the inference of the CMB angular power spectrum. The relativistic particles are fed from the central supermassive blackholes via radio jets leading to radio lobes expanding to megaparsec scales into the intergalactic medium. Using a model of radio galaxy, we model the energetics and the pressure of the non-thermal electrons. We calculate the mean global non-thermal y -distortion, $\langle y \rangle_{NT}$. For observationally reasonable distribution of the jet luminosities in the range of $10^{45} - 10^{47}$ ergs $^{-1}$, we find $\langle y \rangle_{NT}$ to be less than 10^{-5} , and hence not violating the COBE limit as previously claimed. Using the unique spectral dependence of the non-thermal SZ, we show that a detection of $\langle y \rangle_{NT}$ can be within reach at the level of $\gtrsim 5\sigma$ from a future PIXIE-like experiment. The total non-thermal SZ power spectrum, C_{ℓ}^{NT} , from the radio lobes is shown to peak at $\ell \sim 3000$ with an amplitude $\sim 1\%$ of thermal SZ power spectrum from galaxy clusters, and is also within the reach for a PIXIE like experiment. Finally, we show that a detection of the C_{ℓ}^{NT} with a PIXIE-like experiment can lead to $\sim 5\sigma$ constraint on the mass dependence of the jet luminosity with the constraint becoming, at least, ten times better for the proposed more ambitious CMB-HD survey. This will, further, lead to the tightest constraint on the central black hole mass -to-host halo mass scaling relations.

Key words: Cosmology - Cosmic Microwave Background; Cosmology - Theory

1 INTRODUCTION

The precise measurement of primary cosmic microwave background (CMB) anisotropy by Planck (Aghanim et al. 2020) has established the standard model of cosmology. Current and proposed CMB experiments, in the post Planck era, have three main goals: (i) measuring the B-mode primordial CMB polarization (Kamionkowski et al. 1997; Hu & White 1997; Ade et. al. 2021), (ii) measuring pre-recombination spectral distortions of the CMB (Chluba & Sunyaev 2012; Chluba et. al. 2021), and (iii) measuring small angular scale temperature fluctuations (below a few arc minutes) known as the 'Secondary CMB anisotropies' (Hu 2000; Aghanim et al. 2008) caused by the interaction of the CMB photons

with the matter in the line of sight. After decoupling with the background electrons, the CMB photons freestream to us. Along the way, they get scattered by the electrons inside the cosmic structure which imprint a characteristic spatial anisotropy and spectral feature which depends on the energetics, densities and velocity fields of these electrons. We define secondary CMB anisotropies to be all temperature fluctuations generated after the decoupling.

The cosmological sources of secondary CMB anisotropies, as defined above following Aghanim et al. (2008), includes: (i) the late time Integrated Sachs-Wolfe (late-ISW) effect (Sachs & Wolfe 1967) due to the CMB photons travelling through a time-dependent gravitational potential in a recent dark energy dominated universe. (ii) the Rees-Sciama effect (Rees & Sciama 1968) due to the CMB photons traversing a non-linear gravitational potential as largest scale structures get formed, (iii) the gravitational lensing (Lewis & Challinor 2006) due to the large scale structure which conserves total power in the temperature fluctuations but transfers power from

* E-mail:sandeep.acharya@manchester.ac.uk

† E-mail:subha@tifr.res.in

‡ biman@rri.res.in

large angular scales to smaller scales, (iv) the thermal Sunyaev-Zeldovich (tSZ) effect (Zeldovich & Sunyaev 1969) due to scattering of CMB photons by hot (\sim keV) electrons in cosmic structures, and (v) the kinetic SZ effect (kSZ) (Sunyaev & Zeldovich 1980; Ma & Fry 2002) due to doppler boosting by bulk flow of electrons which has contribution from both pre-reionization and post-reionization universe (McQuinn et al. 2005; Shaw et al. 2012; Natarajan et al. 2013). Within the umbrella of SZ effect, different sources of distortions can give rise to a zoo of secondary CMB anisotropies (for example, from quasar bubbles (Aghanim et al. 1996), quasar outflows (Natarajan & Sigurdsson 1999), galactic winds (Majumdar et al. 2001), etc. Apart from temperature anisotropies, there can be generation of polarization anisotropy due to scattering of the CMB photons with the electrons during reionization (Zaldarriaga & Seljak 1997; Hu 2000). These electrons can scatter the CMB photons out of line of sight which damps the primary temperature anisotropy while the quadrupole moment due to CMB hot/cold spots generate E and B-mode polarizations which boosts the polarization power at the horizon scale at reionization. Moreover, power from E-mode, generated at $z \sim 1000$, can leak to B-mode polarization if reionization is anisotropic (Dvorkin et al. 2009; Mukherjee et al. 2019; Roy et al. 2021). The temperature and polarization secondary CMB anisotropies carry invaluable information on the formation and evolution of large scale structures and the baryonic physics over cosmic time and, hence, can be used to probe the sources of the secondary anisotropies.

The thermal SZ effect, due to its redshift independent nature and due to analytic prediction of spectral shape (Zeldovich & Sunyaev 1969), has been thoroughly studied (Fixsen et al. 1996). The most important of the tSZ effect comes from upscattering of CMB photons by the hot intracluster medium, imprinting a distinctive spectral distortion called the y -distortion, the shape of which depends upon the Compton scattering kinematics (Zeldovich & Sunyaev 1969). The mean y -distortion and the angular power spectrum of the tSZ effect has emerged as a powerful tool for cosmological and astrophysical constraints (Majumdar & Subrahmanyan 2000; Komatsu & Kitayama 1999; Birkinshaw 1999; Majumdar 2001b; Komatsu & Seljak 2002; Hill & Pajer 2013; Planck Collaboration & Aghanim et al. 2016; Bolliet et al. 2018; Schaan et al. & Atacama Cosmology Telescope Collaboration 2021; Reichardt et al. 2021; Holder & Chluba 2021; Lee et al. 2021) due to its sensitivity to the expansion history and growth of structures. The spectral shape also carries information on the energetics of electrons inside these structures which can deviate from the fiducial y -distortion due to relativistic electrons (Itoh et al. 1998; Challinor & Lasenby 1998; Sazonov & Sunyaev 1998; Dolgov et al. 2001) which can have implications for cosmological analysis (Remazeilles et al. 2019). Finally, the spectral distortion can also be an ideal tool to detect any departure from the assumption of a thermal nature of the electrons within cosmic structures (Enßlin & Kaiser 2000; Majumdar 2001a).

One possible source of non-thermal relativistic electrons could be radio galaxy cocoons/lobes where relativistic particles are supplied by a central supermassive black hole via radio jets (Felten & Rees 1969; Scheuer 1974; Begelman & Cioffi 1989; Nath 1995). The energetic particles push out the surrounding gas with the radio lobe expanding from hundreds of kpc to Mpc length scales (Kaiser et al. 1997; Acharya et al. 2021). The same population of electrons that are responsible for radio emission also leads to X-ray emission. These have been now detected and can be explained as inverse Compton scattering of CMB photons by the relativistic electrons (Croston et al. 2005; Erlund et al. 2008; Fabian et al. 2009; Johnson

et al. 2007; Isobe et al. 2009). One then naturally expects a spectral signature in the CMB, within the frequency range 10–1000 GHz, due to scattering by the non-thermal electrons. Such non-thermal SZ signature from radio galaxies has been studied in Colafrancesco (2008); Colafrancesco & Marchegiani (2011) by inferring the energy spectrum of non-thermal electrons from X-ray detection. This, however, requires extrapolation of the energy spectral slope at high energies (inferred from Xrays) down to lower energies. In this regard, a detection of any SZ signature can constrain the low energy spectrum independently. Such a detection of non-thermal SZ has been now been claimed by Malu et al. (2017). Recently, Acharya et al. (2021) used a physical model for the evolution of radio galaxy lobes and applied it to predict the resultant CMB distortions and radio luminosities. They showed that the above detection of non-thermal SZ, along with the observed radio luminosity, can be used to constrain radio galaxy models as proposed by Kaiser et al. (1997) and Nath (2010). For example, Acharya et al. (2021) were able to constrain, for the first time, the low energy threshold of non-thermal electron spectrum (p_{min}) which is of the order $\sim 1 - 2$.

In this work, we take the next step and consider the implications for a ubiquitous large scale distribution of radio galaxy cocoons/lobes. Previously, Yamada et al. (1999) and Majumdar (2001a) have looked at the mean spectral distortion signal from a distribution of radio galaxies. Whereas Majumdar (2001a) finds mean y -distortion of $\sim 6 \times 10^{-7}$ for Λ CDM universe, Yamada et al. (1999) found that results violate the Cosmic Background Explorer(COBE)-Far Infrared Absolute Spectrophotometer(FIRAS) (Fixsen et al. 1996) bound. However, the range of values for the luminosity of central engine chosen in that paper appears to be too high (Hardcastle & Croston 2020). Majumdar (2001a) also estimated the power spectrum of CMB anisotropy by radio galaxy cocoons and found the Poisson power spectrum to peak at $\ell \sim 4000$. None of the previous papers do a careful calculation of non-thermal spectral distortion, and comparison to COBE-FIRAS limits are thus naive. We revisit these calculations with more reasonable, observationally motivated, radio galaxy models (Sec 2) and accurate use of non-thermal spectral distortion. Using a halo occupation distribution (HOD) model of radio galaxies (Sec. 3), we compute globally averaged CMB spectral distortion (Sec. 4). We also find the magnitude of the mean distortion signal turns out to be significantly smaller compared to Yamada et al. (1999) for radio galaxies extending up to \sim Mpc scales.

We also compute the non-thermal secondary power spectrum (Sec. 6) due to distortions of the CMB by these radio galaxies and compare them to thermal SZ power spectrum from galaxy clusters. The non-thermal SZ power spectrum turns out to be \sim few percent of the SZ power spectrum from galaxy clusters. This indicates that along with other contributions to the total CMB power spectrum, say from clustering of dusty star forming galaxy (refer to top-left panel of Figure 2 in Reichardt et al. (2021)), the non-thermal SZ power spectrum must be considered for unbiased estimation of cosmological parameters. We look into the impact on cosmological parameters constrained from current SZ experiments in greater detail in a follow-up paper.

Finally, we also discuss the non-thermal distortions in the context of future CMB experiments (Sec. 5, 7) and show that there is a reasonable chance for their detection. We conclude (Sec. 8) by doing a rough estimate of the constraining power of such a detection on cosmology, radio galaxy HOD and radio galaxy physics. In the rest of the paper, we use parameters listed in Table 1 (Aghanim et al. 2020) as the fiducial cosmological model.

Cosmological parameters	1 σ value
Ω_m	0.3111 \pm 0.0056
Ω_Λ	0.6889 \pm 0.0056
H_0	67.66 \pm 0.42
n_s	0.9665 \pm 0.0038
$10^9 A_s$	2.105 \pm 0.030
σ_8	0.8102 \pm 0.006

Table 1. A few of measured and derived cosmological parameters which are most relevant for computing C_ℓ of radio galaxies. We have used the values of (Aghanim et al. 2020).

2 MODEL FOR EVOLVING RADIO GALAXY LOBES

In our model of radio galaxy, non-thermal relativistic electrons are ejected with a jet luminosity (Q_j) and jet lifetime (t_j)¹. The jet remains active for $\approx 10^7 - 10^8$ yr after which the jet becomes inactive. The jet pushes out the surrounding gas and forms a radio lobe. The density profile of the surrounding gas can be written as, $\rho(r) = \Lambda r^{-2}$, with $\Lambda = 10^{19} \text{ g cm}^{-3}$ (Fukazawa et al. 2004; Jetha et al. 2007). The non-thermal electron energy distribution in the radio lobe is given by a power law with, $n(\gamma_i, t_i) = n_0 \gamma_i^{-\alpha_p} d\gamma_i$, where γ_i is the Lorentz factor of electrons at time of injection t_i , and α_p is the spectral index. The maximum γ is assumed to be $\gamma_{\max} = 10^6$. The evolution of the radio galaxy can be described by (Reynolds & Begelman 1997),

$$Q_j(t) = \frac{1}{\Gamma_c - 1} (V_c \dot{p}_c + \Gamma_c p_c \dot{V}_c), \quad \frac{dL_j}{dt} = \left(\frac{p_c}{\rho} \right)^{1/2}, \quad (1)$$

where $Q_j(t)$ is the jet luminosity which is non-zero when jet is on ($t < t_j$, where t_j is the jet lifetime) and zero for $t > t_j$, $\Gamma_c = \frac{4}{3}$, V_c is the volume of the radio lobe, p_c is the pressure in the radio lobe, L_j is the fiducial size of the lobe and ρ is the density of surrounding gas. We assume the axial ratio of the cylinder shaped radio lobe to be $R = 2$, the average observed ratio (Leahy & Williams 1984). The volume of the lobe is then given by,

$$V_c = \frac{\pi}{4R^2} L_j^3. \quad (2)$$

The magnetic and particle energy densities in the lobe are given by,

$$U_B(t) = \frac{Ap_c(t)}{(\Gamma_c - 1)(1 + A)}, \quad U_e(t) = \frac{p_c(t)}{(\Gamma_c - 1)(1 + A)}, \quad (3)$$

where $A = (1 + \alpha_p)/4$ (Kaiser & Alexander 1997).

The non-thermal electrons cool via adiabatic expansion, synchrotron emission and by inverse Compton cooling off the CMB. The equation for evolution of electron Lorentz factor γ is given by,

$$\frac{d\gamma}{dt} = -\frac{1}{3} \frac{1}{V_c} \frac{dV_c}{dt} - \frac{4}{3} \frac{\sigma_T}{m_e c} \gamma^2 (U_B + U_C), \quad (4)$$

where σ_T is Thomson cross-section, m_e is the mass of electron, c is the speed of light, U_B , U_C are the magnetic energy density and CMB energy density, respectively. Due to the γ^2 factor in Eq. 4, the most energetic electrons in the jet cool very fast. The lowest energy electrons survive for long and these electrons are responsible for creating distortion in the CMB field which has a characteristic shape depending upon the spectrum of non-thermal electrons (Colafrancesco 2008; Acharya et al. 2021). In this work, we have assumed $\alpha_p = 3$, though, the spectral distortion shapes are not sensitive to small changes to α_p .

¹ For choice of Q_j & t_j , see discussion in Section 4.

3 MODELING THE DISTRIBUTION OF RADIO GALAXIES INSIDE DARK MATTER HALOS

To calculate the impact of a large scale spatial distribution of radio galaxies on the secondary CMB anisotropies, we need to first compute the cosmological distribution of radio galaxies in the universe. For this, we use the halo model to associate radio galaxies with parent dark matter halos. The abundance of the parent halos is described by the halo mass function (for a particular overdensity Δ) given by,

$$\frac{dn}{dM_\Delta} = f(\sigma, z) \frac{\rho_{m0}}{M_\Delta} \frac{d\ln \sigma^{-1}}{dM_\Delta}, \quad (5)$$

We follow Tinker et al. (2008, 2010) expression for $f(\sigma, z)$ given by

$$f(\sigma, z) = A \left[\left(\frac{\sigma}{b} \right)^{-a} + 1 \right] e^{-(c/\sigma^2)} \quad (6)$$

The parameters with their redshift dependence is tabulated in their paper. Tinker et al. (2008) provide mass function for different overdensity w.r.t mean matter density while our mass function is defined at overdensity of 500 w.r.t the critical energy density which amount to $500/0.3 \approx 1600$ overdensity w.r.t to mean matter density. The The value of r_{500} can then be directly computed as $M_{500} = \frac{4\pi}{3} \rho_c \times 500 \times r_{500}^3$. From here on, we drop the subscript Δ and simply refer to mass function as dn/dM . Note, that in Sec 6, the universal pressure profile used for computing the thermal SZ from galaxy clusters is given in terms of M_{500} . The mass variance $\sigma(z)$ can be computed from linear matter power spectrum with $\sigma(z) = D(z)^2 \sigma_{z=0}$. $D(z)$ is the linear growth factor normalized to unity at $z = 0$. The mass variance σ is a function of smoothing scale R and is given by

$$\sigma(R) = \frac{1}{2\pi^2} \int dk k^2 P(k) \left[\frac{3j_1(kR)}{kR} \right]^2, \quad (7)$$

where $P(k)$ is the matter power spectrum which we obtain using publicly available code CLASS (Blas et al. 2011).

Although the mass function described above gives the abundance of dark matter halos, one still has to associate radio galaxies to their host halos, i.e find a suitable fraction $F(M)$, to get the mean abundance of radio galaxies. In Yamada et al. (1999) and Majumdar (2001a), a mass independent $F(M)$ was a taken to be 0.01, i.e 1% of the halos in the mass-range $(10^{12} - 10^{14}) \text{ M}_\odot$ are assumed to host radio galaxies. The value of $F(M) = 0.01$ was arrived through looking at the ratio of the total integrated radio luminosity -to- optical luminosity of galaxies with a magnitude cut of $M_V < -22$ as the upper limit.

In our work, we use the halo occupation distribution (HOD) to link radio galaxies to their host halos (Wake et al. 2008; Smolčić et al. 2011). Below, we briefly describe their main results that we adopt and urge the reader to look up their papers for details. In Smolčić et al. (2011), the radio galaxy fraction is given by

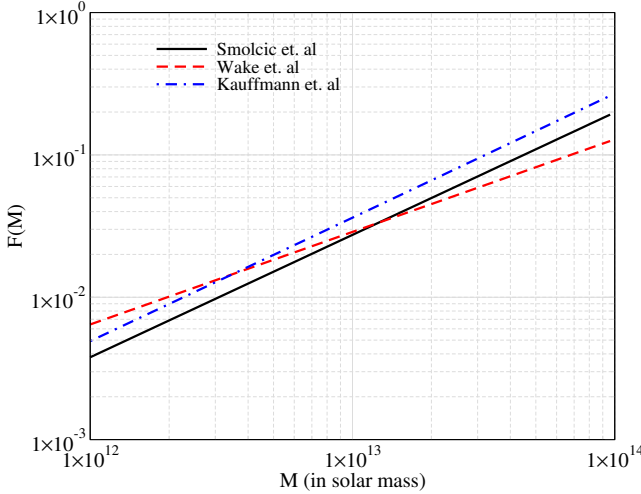


Figure 1. The host halo mass dependence of radio galaxy fraction ($F(M)$)

$F(M) = A_{\text{HOD}} \left(\frac{M}{10^{13.6} M_{\odot}} \right)^{\beta}$, with the fiducial value of $A_{\text{HOD}} = 0.09$ and $\beta = 0.86$. As before, we assume that the radio galaxies reside inside dark matter halos with mass $10^{12} - 10^{14} M_{\odot}$ and use this HOD fit in this mass regime. A similar radio galaxy fraction was previously given in Wake et al. (2008) where $F(M) = 0.02 \left(\frac{M}{4 \times 10^{12} M_{\odot}} \right)^{0.65}$. The halo mass in Smolčić et al. (2011) is defined w.r.t r_{200} or the radius within which the density of mass is 200 times the critical density. We convert it to M_{500} using the transformation given in Hu & Kravtsov (2003) and using the concentration relation of Duffy et al. (2008).

We also follow another alternate route, based on a modification of the initial approach taken by Yamada et al. (1999), to estimate the number of radio galaxies inside a halo of mass M . The average number of galaxies as a function of dark matter halo has been formulated in semi-analytic galaxy formation models (Kauffmann et al. 1999; Berlind et al. 2003). In these models, the number of galaxies depends upon galaxy type and luminosity. The number of blue galaxies is given by $N_{\text{blue}} = 0.7$ if $M_{\text{halo}} < M_{\text{blue}}$ else $N_{\text{blue}} = 0.7 \left(\frac{M_{\text{halo}}}{M_{\text{blue}}} \right)^{0.8}$ with $M_{\text{blue}} = 4 \times 10^{12} h^{-1} M_{\odot}$ (Cooray & Sheth 2002). Similarly, the number of red galaxies is given by $N_{\text{red}} = \left(\frac{M_{\text{halo}}}{M_{\text{red}}} \right)^{0.9}$ with $M_{\text{red}} = 2.5 \times 10^{12} h^{-1} M_{\odot}$ if $M_{\text{halo}} > 10^{11} h^{-1}$ solar mass. We assume the number of radio galaxies to be $F(M) = 0.01 \times (N_{\text{blue}} + N_{\text{red}})$ to represent the fraction of number of radio galaxies with respect to sum of total number of red and blue galaxies. We plot the different mass dependent radio galaxy fractions discussed above in Fig. 1. They agree with each other within a factor of 2 at the two mass ends, and better within.

In Fig. 2, we plot the z -dependent number density of radio galaxies given by

$$\frac{d^3 N}{dM dz d\Omega} = \frac{d^2 V}{dz d\Omega} \frac{dn(z)}{dM} F(M), \quad (8)$$

where $\frac{d^2 V}{dz d\Omega} = \frac{\chi^2(z)}{H(z)}$, $\chi(z)$ is the comoving distance to redshift z and dn/dM is the mass function defined in Eq. 5. We have normalized the matter power spectrum such that $\sigma_8 = 0.81$.

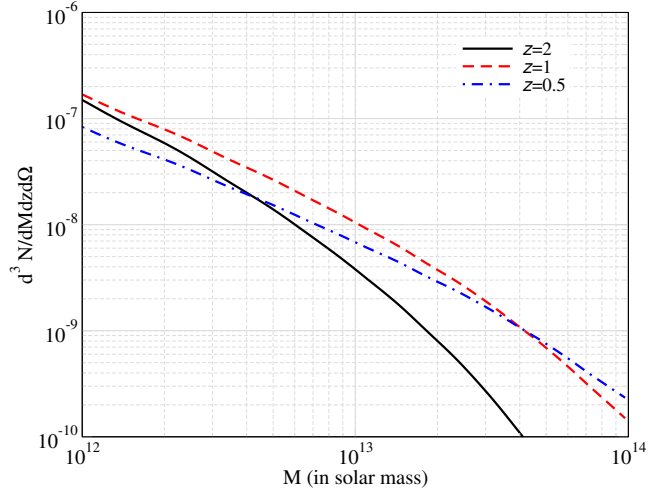


Figure 2. Radio galaxy space density, $\frac{d^3 N}{dM dz d\Omega}$, as a function of host halo mass for three different redshifts.

4 THE GLOBAL CMB DISTORTION FROM COSMOLOGICAL DISTRIBUTION OF RADIO GALAXIES

In this section, we calculate the cumulative global CMB distortion from a cosmological distribution of radio galaxies. To avoid confusion between thermal and non-thermal SZ distortions, we will use y_T parameter (or $\langle y \rangle_T$ for mean) to denote thermal SZ distortions and y_{NT} (or $\langle y \rangle_{\text{NT}}$ for mean) for non-thermal SZ distortions. Without doing a full calculation, it is easy to estimate an upper limit on $\langle y \rangle_{\text{NT}}$. This can be obtained by comparing with the maximum limit on the mean CMB distortions coming from the COBE-FIRAS experiment (Fixsen et. al 1996) given by $\langle y \rangle_{\text{COBE}} \leq 1.5 \times 10^{-5}$ at 2σ . While the mean SZ distortion from galaxy clusters is very close to COBE y -distortion limits (with minor relativistic corrections (Itoh et al. 1998; Challinor & Lasenby 1998; Sazonov & Sunyaev 1998)), the comparison is straight-forward since the SZ distortion in clusters comes from a thermal population of electrons. In contrast, the non-thermal SZ distortion, in this study, comes from a non-thermal population of electrons and the spectral shapes of CMB distortion from non-thermal -vs- thermal electrons can be vastly different for the same y -distortion (Colafrancesco 2008; Acharya et al. 2021). More concretely, the distortion in CMB intensity can be written as, $\Delta I(x) = y g(x)|_{\text{T/NT}}$, where the y -parameter depends upon the number density and the spatial distribution of the energetic electrons (which can be same for thermal and non-thermal electrons) whereas the spectral factor $g(x)$ captures the information regarding the energy distribution of electrons. This is shown in Fig. 3, where we compare the spectral distortion shapes for thermal and non-thermal SZ distortions for different non-thermal electron population. Please see also figure 2 in (Acharya et al. 2021).

Due to the significant difference in the spectral shapes, the constraint on the non-thermal SZ distortion, when compared with COBE-FIRAS limits, needs to be estimated carefully. The total intensity can be written as (Fixsen et. al 1996),

$$I(\nu) = B_{\nu}(T_0) + \Delta T \frac{\partial B_{\nu}}{\partial T} + G_0 g(\nu) + A \Delta I(\nu), \quad (9)$$

where $B_{\nu}(T_0)$ is the Planck spectrum at temperature T_0 . The second term captures the temperature shift of the CMB i.e. this term

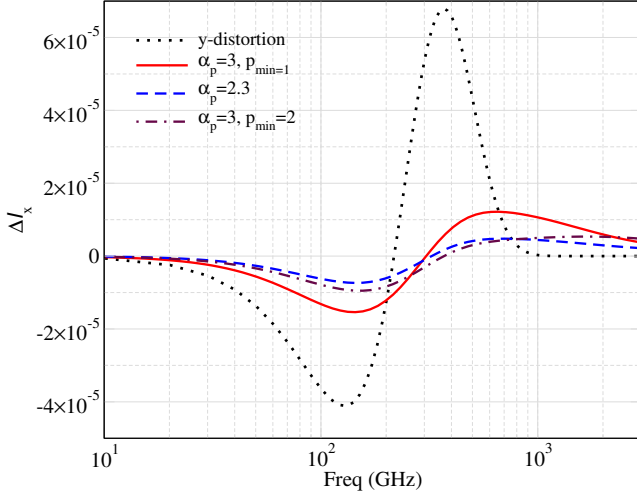


Figure 3. Non-dimensional intensity $\Delta I_x (= x^3 \Delta n)$ of spectral distortion as a function of frequency $\nu = 56.75 \times x$ GHz where $x = \frac{h\nu}{k_B T_{\text{CMB}}}$ from thermal and different non-thermal electron population with the same y -parameter= 10^{-5} . Here $p_{\min} = \sqrt{\gamma_{\min}^2 - 1}$ when γ_{\min} is the minimum energy and α_p is the spectral index of the non-thermal electron energy distribution is as shown in the plot.

is non-zero if the CMB temperature is different from T_0 . The third term is the galactic spectrum which is given in Fixsen et. al (1996) and the last term is the modelled deviation which in our case will be the non-thermal SZ signal. To proceed, we use the residuals (i.e $I(\nu) - B_\nu(T_0)$) given in Table 3 of Fixsen et. al (1996) and fit the linear combination of the temperature shift, our non-thermal spectrum and a galactic spectrum and obtain the best fit values for the corresponding amplitude i.e. $\Delta T, G_0$ and A . We obtain a 2σ upper limit on y -parameter for the non-thermal spectrum to be 1.2×10^{-4} . The higher value of the estimated y -distortion, compared to thermal y -distortion, is expected as the peak intensity of non-thermal spectrum is more than a order of magnitude lower than the thermal spectrum for the same y -parameter as can be seen in Fig. 3.

The cosmology and radio galaxy physics dependent $\langle y \rangle_{NT}$ from a cosmological distribution of cocoons is given by

$$\langle y \rangle_{NT} = \int \int \int F(M) \frac{p_c}{m_e c^2} L_J \sigma_T \frac{dn}{dM}(M, z_{st}) \times \frac{L_J^2}{d_A^2} \frac{d^2 V}{dz d\Omega} dz dz_{st} dM, \quad (10)$$

where $\frac{dn}{dM}$ is the comoving number density of the dark matter halos which is given by the halo mass function in Eq. 5, z_{st} is the starting redshift of jet, d_A is the angular diameter distance ($d_A = a\chi$) where $a(z)$ is the scale factor and $\chi(z)$ is the comoving distance, and $\frac{d^2 V}{dz d\Omega}$ is the comoving volume element. We consider a cosmological distribution of radio galaxy with z_{st} varying from 0 to 4.

Motivated by theoretical modeling and observational evidence connecting central blackhole feedback to host halo mass (for example, see Nath & Roychowdhury (2002); Iqbal et al. (2018)), we take the jet luminosity to scale linearly with the mass of the dark matter halo such that the luminosity of the radio galaxies inside a dark matter halo with mass M is given by, $Q_J = 10^{45} \left(\frac{M}{10^{12} M_\odot} \right)^{\alpha_M}$ (with $\alpha_M = 1$) ergs $^{-1}$ unless otherwise mentioned. Therefore, our fiducial radio galaxy luminosity varies between $10^{45} - 10^{47}$ ergs $^{-1}$. The highest observed radio galaxy luminosity turns out to be few times 10^{47} ergs $^{-1}$ (Hardcastle & Croston 2020).

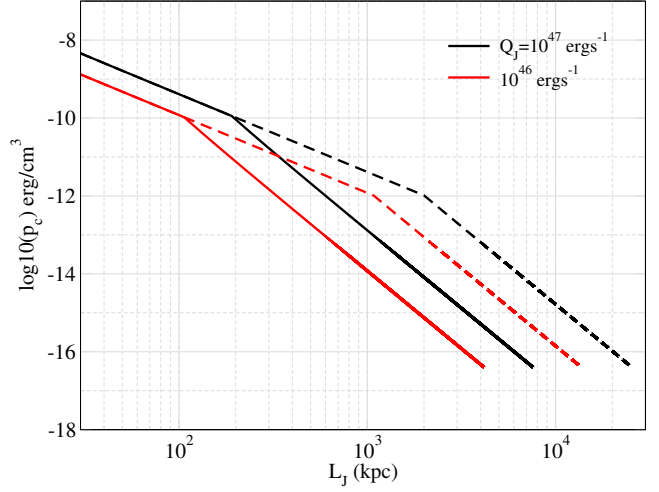


Figure 4. Pressure of the non-thermal electrons as a function of the size of radio galaxy lobes. We show the evolution of a radio galaxy with different Q_J and lifetimes 10^7 yr (solid), 10^8 yr (dashed) with $z_{st} = 1$.

Estimates of the duration of the active phase of jets in radio galaxies, from observations of spectral aging, show that t_J lies between $10^7 - 10^8$ yrs (see, e.g., Konar et al. (2013)). Also, spectral aging and lobe expansion speed arguments typically estimates an active timescale of a few $\times 10^7$ yrs ((Alexander & Leahy 1987; Shabala et al. 2008)). Moreover, simulations have also suggested that jets become disrupted after a timescale of order of 10^8 yr (Tucker & David 1997; Omma & Binney 2004). For the sake of simplicity, we assume that all the radio galaxies have same lifetime and do not have a distribution, and chose our fiducial t_J to be 10^8 yrs. However, we show the dependence of the luminosity and jet lifetime on the pressure as function of the size of the cocoon in Fig 4.

Based on a systematic study of radio galaxies using Suzaku, Isobe & Koyama (2015) have catalogued radio lobes of varying sizes going up to 5Mpc, which we use as an upper limit on the cocoon size. Note, however, that it is still possible for cocoons to grow to even larger sizes without the hard cutoff. It is evident from Fig 4 that, irrespective of the luminosity or jet lifetime, the cocoon pressure falls by 2 – 5 orders of magnitude from its initial value. As seen in Fig. 5, the product of pressure and volume keeps on increasing until the jet stops at which point pressure drops dramatically and the product starts to fall off. Combined with eq. 10, it is easy to see that $\langle y \rangle_{NT}$ receives largest contribution for Δz starting with z_{st} and until the jet stops, for one radio galaxy with a given z_{st} or for a cosmological ensemble of radio galaxies. For a given luminosity, the jet expands more for a higher lifetime and the product of pressure and volume is higher (see Fig. 5). For an ensemble of galaxies, the larger CMB distortion from large cocoons fuelled by larger luminosities are strongly diluted by the exponential fall in the number of higher mass halos. However, some uncertainty due to our incomplete knowledge of jet lifetime remains.

We plot the cumulative y_{NT} from radio galaxies for few different radio galaxy lobes model parameters in Fig. 6. For comparison with Yamada et al. (1999), we also do a calculation with jet luminosity parameter as chosen by these authors to vary between $2 \times 10^{47} - 2 \times 10^{49}$ ergs $^{-1}$. As we increase the jet luminosity and jet lifetime, the pressure increases as expected, and we get larger y_{NT} which can be in conflict with the maximum $\langle y \rangle_{NT}$ estimated above based on COBE-FIRAS limits (for example, see black solid

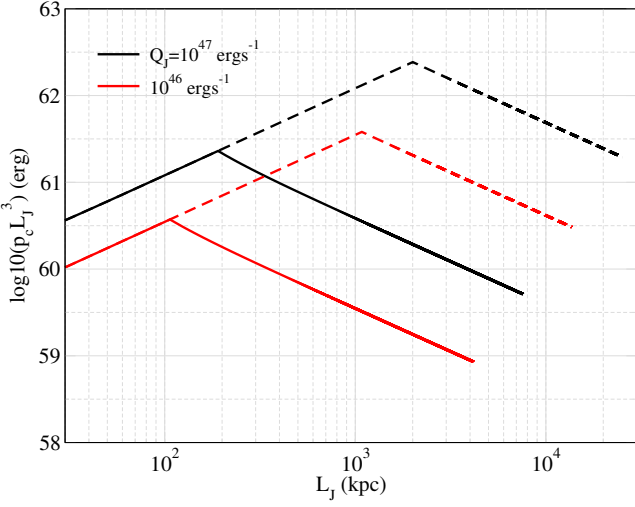


Figure 5. The product of pressure and volume of a radio galaxy lobe with same parameters as in Fig. 4.

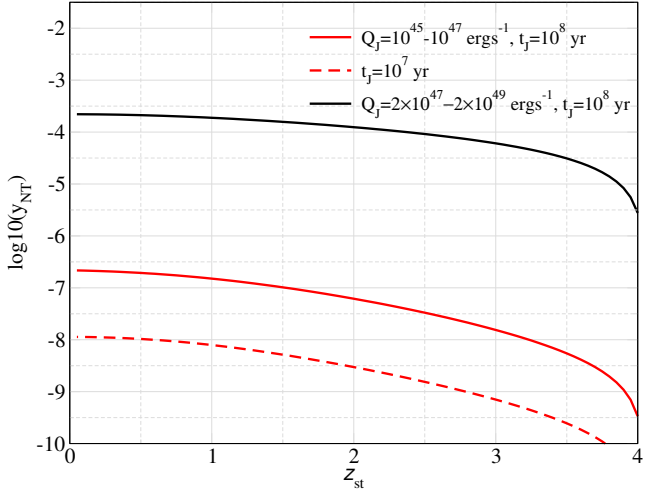


Figure 6. The cumulative mean CMB distortion $\langle y \rangle_{NT}$ from radio galaxies for different jet lifetimes and jet luminosity range.

line in Fig. 6. Using a more physically motivated maximum cocoon size of 5 Mpc, the estimated $\langle y \rangle_{NT}$ is shown in Fig. 6 which are significantly smaller. Yamada et al. (1999) obtained an estimate for $\langle y \rangle_T$ (and not $\langle y \rangle_{NT}$) to be greater than 10^{-5} for a cosmological distribution of radio galaxies which is in conflict with COBE-FIRAS (Fixsen et. al 1996). With our analytic evolution model of radio galaxies along with recent estimation of the radio galaxy fraction in massive halos, we see that $\langle y \rangle_{NT}$ is several orders of magnitude smaller. Thus, we conclude that there are no constraints on radio galaxy models from COBE-FIRAS (Fixsen et. al 1996) data.

5 DETECTING THE GLOBAL CMB DISTORTION

5.0.1 Detecting the non-thermal SZ distortion

After calculating the mean secondary non-thermal SZ distortion (ntSZ) from a population of radio galaxy cocoons in the last section, we now focus on the prospect of detecting $\langle y \rangle_{NT}$ in future.

To proceed, we first plot the predicted cosmological signals and the foregrounds in Fig. 7. We consider a total of 10 foregrounds, listed in Table 1 of Abitbol et al. (2017) which are divided into two types. The cosmological foregrounds, which we discuss below, are y and μ -distortions, relativistic SZ (rSZ) and temperature shift of CMB black body. The astrophysical foregrounds are dust, cosmic infrared background, synchrotron, free-free, CO and spinning dust (AME). Since, we are interested at the prospects of a future detection, we focus on the Primordial Inflation Explorer (PIXIE)-like observational program, and also show the instrumental noises for PIXIE (Kogut et. al 2011) and super-PIXIE. In particular, PIXIE has 400 frequency channels from 15 GHz to 6000 GHz which are equally placed at 15 GHz intervals. However, above 3000 GHz, the experimental noise starts to increase rapidly and, hence, we consider 200 channels from 30 GHz to 3000 GHz in our analysis.

We consider the temperature shift (ΔT) of the CMB spectrum arising from the uncertainty in accurately measure the CMB temperature, y -distortion from galaxy clusters and μ -distortion from pre-recombination adiabatic cooling (Sunyaev & Zeldovich 1970; Chluba & Sunyaev 2012) as sources of cosmological signals in standard cosmology. The mean value of $\langle y \rangle_T$ from galaxy clusters in the universe is taken to be $\sim 1.8 \times 10^{-6}$ (Hill et al. 2015). As the mean temperature of hot gas in these galaxy clusters can be ~ 1 keV, relativistic correction (Itoh et al. 1998; Challinor & Lasenby 1998; Sazonov & Sunyaev 1998; Dolgov et al. 2001) to non-relativistic y -distortion becomes appreciable which we also include here. We parameterize this as rSZ with its amplitude being the same as the y -distortion. There can be other sources to y -distortion from exotic physics such as dark matter decay and annihilation (Sarkar & Cooper 1984; Chluba & Sunyaev 2012; Khatri et al. 2012; Chluba et al. 2012); however, we ignore such non-standard sources in this work. The amplitude of μ -distortion expected from adiabatic cooling of electrons in the standard cosmology is $\sim 2 \times 10^{-8}$ (Chluba 2016). Another source of CMB distortion in the standard cosmology is from cosmic recombination at $z \sim 1000$ (Dubrovich 1975; Sunyaev & Chluba 2009; Hart et al. 2020). The amplitude of the signal is of the order 10^{-9} and is expected to be uncorrelated with other cosmological signals due to complicated frequency dependence. We ignore this signal in this work. For the non-thermal SZ signal from radio galaxies, we consider a fiducial $\langle y \rangle_{NT} = 5 \times 10^{-8}$ with the spectral index of electrons, α_p , equal to 3. Having the signal and all the foregrounds in place, we first do a fit of the non-thermal SZ in terms of $\langle y \rangle_T$, μ and temperature shift of the CMB and throw out the best fit, i.e., we write,

$$\Delta I_{ntSZ} = A_T \Delta I_T + A_y \Delta I_y + A_\mu \Delta I_\mu + A_{rSZ} I_{rSZ}, \quad (11)$$

where A_T , A_y , A_μ and A_{rSZ} are free parameters which can have any values and have nothing to do with the values expected from standard cosmology. By throwing out the best fit from non-thermal SZ, we have a residual non-thermal SZ signal which is independent of the linear combination of the other cosmological signals. We consider this to be the relevant non-thermal SZ signal that needs to be detected and look for its detectability using a Fisher matrix approach. We, further, compare these results with the case when the best fit is not removed.

The expression for Fisher matrix is given by (Tegmark et al. 1997; Matsubara 2004),

$$F_{\alpha\beta} = \sum_i \frac{\partial \Delta I}{\partial \Delta \alpha} \frac{1}{\delta I^2(\nu)} \frac{\partial \Delta I}{\partial \Delta \beta}, \quad (12)$$

where, for us, α, β are model parameters such as amplitudes of cosmological and astrophysical foregrounds and $\delta I(\nu)$ is the PIXIE

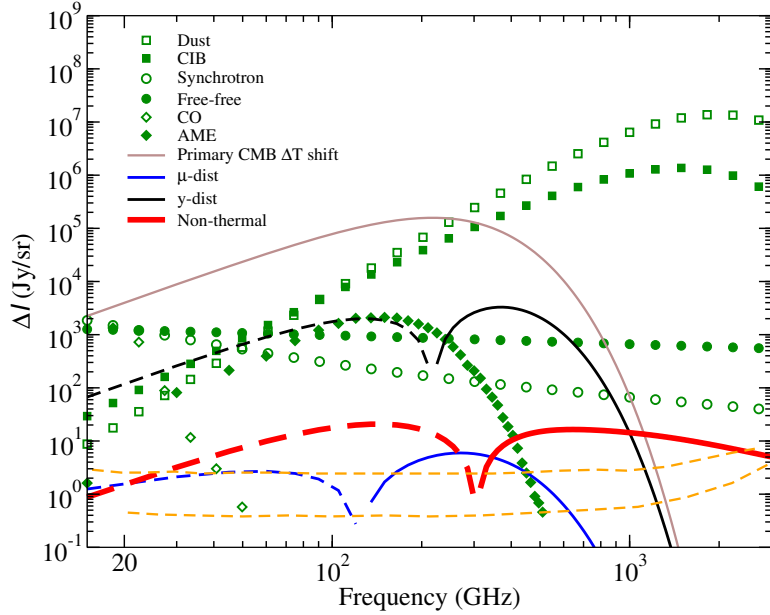


Figure 7. The ntSZ distortion intensity (in Jansky per steradian) and frequency dependence in the context of other cosmological signals and foregrounds. The amplitude of temperature shift, y -distortion, μ -distortion and non-thermal SZ are 1.2×10^{-4} , 1.8×10^{-6} , 2×10^{-8} and 5×10^{-8} respectively (see text for details). The electron spectral index, $\alpha_p = 3$, used for ntSZ. The solid and dotted lines for the cosmological signals refer to positive and negative values respectively. We also show PIXIE and super-PIXIE sensitivities with dashed orange lines.

Case	Best fit removed	Best fit unremoved
$y + \mu + \Delta T$	39σ	39σ
$y + \mu + \Delta T + rSZ$	35σ	35σ
Astro foregrounds	5.38σ	2.8σ

Table 2. Detection forecasts for non-thermal SZ in presence of cosmological and astrophysical foregrounds with PIXIE error bars.

instrument sensitivity with the assumption that the noise covariance matrix is diagonal. We are interested in the marginalized constraints on non-thermal SZ signal. The Fisher matrix can be written as, $\begin{bmatrix} F & B \\ B^T & C \end{bmatrix}$ where F is the submatrix of parameters that we are interested in and C is the submatrix of the parameters that we want to marginalize over and B is correlation matrix elements with our desired parameter. The marginalized Fisher matrix can then be obtained as $F'_{\alpha\beta} = F - BC^{-1}B^T$ (Matsubara 2004).

Since we are interested in the possible detection of the global non-thermal SZ signal, we marginalize over all other parameters other than ΔI_{ntSZ} . For the marginalized Fisher matrix, the signal-to-noise (S/N) is given by \sqrt{F} . The resultant S/N are shown in Table 2 for the scenarios when the best-fit model is subtracted and when it is not. We start with the scenario where there are no astrophysical foregrounds and only cosmological signals (δT , y_{th} & μ) are present in addition to non-thermal SZ signal. In this case, we can detect the global CMB distortions by the radio galaxy cocoons at 39σ significance. The S/N degrades to 35σ when rSZ is added since rSZ has a longer frequency tail. Note, that for low mass clusters ($T_{\text{gas}} \lesssim 5\text{keV}$), rSZ is very similar to the y -distortion. However, the addition of astrophysical foregrounds, with their large amplitudes, degrade the detection significance considerably leaving with the possibility of $\sim 3\sigma$ detection when best-fit is unremoved, which improves to 5.4σ if the best-fit is removed. In conclusion, there appears to be very good possibility of detecting the non-thermal SZ signal with a survey like PIXIE.

5.0.2 Implications for detection of μ -distortion in the presence of non-thermal SZ

Spectral distortions in the CMB during the epoch $2 \times 10^5 \lesssim z \lesssim 2 \times 10^6$ (Chluba & Sunyaev 2012; Khatri & Sunyaev 2012) thermalizes to Bose-Einstein distribution (or μ -distortion) due to efficient scattering between CMB photons and the background electrons which is a photon number conserving process. At higher redshifts, photon non-conserving processes become important which drive the distorted CMB spectrum to a Planck spectrum. In Λ CDM, μ -distortions are generated due to adiabatic cooling of the baryons and from dissipation of primordial small scale perturbations (Hu et al. 1994; Chluba et al. 2012; Khatri et al. 2012). Therefore, detection of μ -distortion probes the expansion history of universe in the radiation dominated era and also probes the initial condition of density fluctuations in the universe. Given the importance of the μ -distortion, we check to see whether the likelihood of detection of the μ -distortion gets significantly degraded when we add the ubiquitous non-thermal SZ to be an extra cosmological foreground. We start by considering the non-thermal SZ to be the only foreground. In this case, the degradation in the detected μ -signal is negligible when considering 200 bands between 30-3000 GHz for a PIXIE like survey. With a lesser coverage of frequency bands, we expect to find more correlation between μ and non-thermal SZ distortion. However, even for a survey with fewer (~ 20) bands between 30-300 GHz, the degradation remains marginal when we include all astrophysical foregrounds

In fact, with 200 frequency bands, the significance of detection

of μ in presence of cosmological foregrounds is $\sim 3\sigma$ irrespective of whether non-thermal SZ is included or not. We also checked the importance of high frequency channels by including or omitting channels between 2000–3000 GHz. The S/N for detecting μ in presence of astrophysical foregrounds (including ntSZ) does improve slightly from 1.25σ to 2.3σ when more channels are added between 2000 to 3000 GHz.

6 THE NONTHERMAL SZ POWER SPECTRUM FROM RADIO GALAXY COCOONS

In the previous sections, we had looked at the mean non-thermal SZ distortion by radio galaxy lobes. A cosmological distribution of radio galaxies will induce spatial fluctuations in the CMB distortions. In this section, we calculate the two point correlation function or power spectrum of ntSZ fluctuations from radio galaxies and compare it to the thermal SZ power spectrum from galaxy clusters. As already pointed out, the radio galaxies are assumed to reside within dark matter halos and, hence, their spatial and redshift distribution follows that of their host halos, and can be analytically written in the same lines as for galaxy clusters. We will first write the the expression for galaxy clusters and modify it to suit radio galaxy lobes.

For the galaxy clusters, the thermal SZ power spectrum can be written as the sum of one halo and two halo terms. The expression for one halo term for galaxy clusters is given by (Molnar & Birkinshaw 2000; Majumdar 2001a; Komatsu & Seljak 2002; Hill & Pajer 2013),

$$C_\ell^{1h} = g_\nu^2 \int dz \frac{d^2V}{dzd\Omega} \int dM \frac{dn(M, z)}{dM} |y_l(M, z)|^2, \quad (13)$$

where g_ν is the value of y -distortion spectral function (Zeldovich & Sunyaev 1969) at a frequency ν , $y_l(M, z)$ is the l -space equivalent of the y -distortion each halo, and the other terms have their usual meanings. For y -distortion, fractional change in intensity $\frac{\Delta y}{y} = \frac{xe^x}{(e^x - 1)^2} [x \coth(x/2) - 4]$ ($x = \frac{hy}{kT_{\text{cmb}}}$) which when converted to fractional change in temperature is given by, $\frac{\Delta T}{T} = [x \coth(x/2) - 4]$, which is the factor g_ν in Eq. 13. The value of g_ν is -2 in the Rayleigh-jeans limit i.e. $x \rightarrow 0$. The corresponding expression for the two-halo term is given by,

$$C_\ell^{2h} = g_\nu^2 \int dz \frac{d^2V}{dzd\Omega} \left[\int dM \frac{dn(M, z)}{dM} b(M, z) y_l(M, z) \right]^2 P_{lin} \left(\frac{l}{\chi(z)} \right), \quad (14)$$

where $P_{lin}(k)$ is the cosmological matter power spectrum in the linear regime and $b(M, z)$ is the dark matter halos bias (Tinker et al. 2010) given by $b(M, z) = 1 + \left(\frac{\delta_c^2}{\sigma(M, z)^2} - 1 \right) / (\delta_c)$ with $\delta_c = 1.686$.

For galaxy clusters, the expression for $y_l(M, z)$ is given by

$$y_l(M, z) = \frac{\sigma_T}{m_e c^2} \frac{4\pi r_{500}}{l_{500}^2} \int dx x^2 \frac{\sin(lx/l_{500})}{lx/l_{500}} P_e(x), \quad (15)$$

where r_{500} defines the cluster centric radius within which the mean density of matter is 500 times the critical energy density of the universe, $x = r/r_{500}$ with r being the radial distance from the center of galaxy cluster. We get r_{500} from the fitting formulae of Hu & Kravtsov (2003). The characteristic multipole, l_{500} , of the pressure profile is given by $l_{500} = a(z)\chi(z)/r_{500}$, where $a(z)$ is the scale factor and $\chi(z)$ is the comoving distance of the cluster at redshift z . The NFW halo is characterized by its concentration parameter, $c(M, z) = r_{vir}/r_s$, where r_s is the scale radius and r_{vir} denoted the

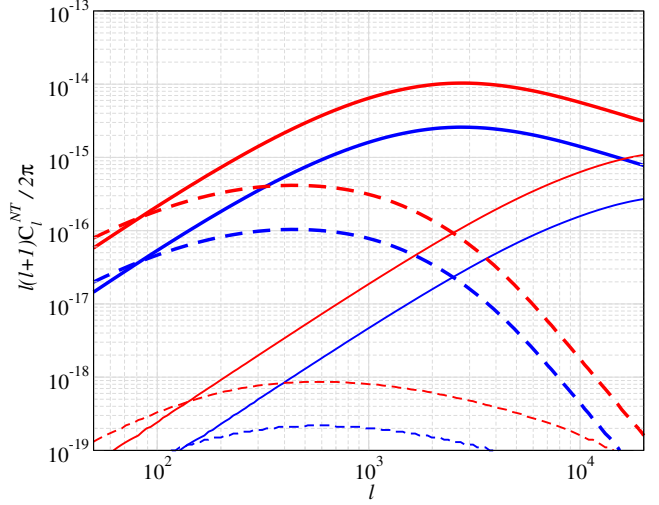


Figure 8. The one-halo (solid lines) and two-halo (dashed lines) ntSZ power spectrum from radio galaxies at 150 GHz. The thicker lines correspond to $t_J = 10^8$ yr and the thinner lines are for $t_J = 10^7$ yr. For both cases, $\alpha_p = 3$ is shown red and 2.3 in blue.

virial radius of the halo. In this work, we use N-body simulations motivated mass-concentration relation (Duffy et al. 2008) given by

$$c(M, z) = 7.85 \left(\frac{M}{2 \times 10^{12} M_\odot h^{-1}} \right)^{-0.081} (1+z)^{-0.71} \quad (16)$$

The CMB distortion by galaxy clusters ultimately depends on the pressure, P_e , of the hot intracluster medium. We use the observationally determined universal pressure profile (Arnaud et al. 2010; Planck 2013) given by

$$P_e(x) = 1.65 \left(\frac{h}{0.7} \right)^2 \left(\frac{H(z)}{H_0} \right)^{8/3} \left[\frac{M_{500}}{3 \times 10^{14} M_{\odot}} \right]^{0.78} \times P_0(c_{500}x)^{-\gamma} [1 + (c_{500}x)^\alpha]^{\gamma - \beta/\alpha} \quad (17)$$

with the best fit parameters taken from Planck (2013). Finally, for the cluster SZ power spectrum, we consider dark matter halos in the mass range of $(10^{13} - 10^{16}) M_\odot$ up to $z \leq 5$. It is well known that for clusters the 1-halo term dominates at all ℓ -range, and the total C_ℓ peaks at $\ell \sim 3000$. This is seen in Figure 8 and 9.

Next, we turn to the radio galaxy ntSZ power spectrum (C_ℓ^{NT}), which has a significantly different spectral shape than thermal y -distortion (see Fig. 3). Note again that we assume the radio galaxy lobes to populate dark matter halos in $(10^{12} - 10^{14}) M_\odot$ mass range and the jet luminosity is assumed to scale linearly with the mass of the halo. The pressure profile, as discussed in Section 2, is assumed to be constant inside the radio galaxy lobe and zero outside. Following the formalism for the galaxy clusters above, we can compute the one-halo and two-halo terms from Eq. 18 and 19 below,

$$C_\ell^{NT,1h} = h_\nu^2 \int dz \frac{d^2V}{dzd\Omega} \int dM F(M) \frac{dn(M, z)}{dM} \int dz_{st} |y_l(M, z, z_{st})|^2, \quad (18)$$

$$C_{\ell}^{NT,2h} = h_{\nu}^2 \int dz \frac{d^2V}{dzd\Omega} \left[\int dMF(M) \frac{dn(M,z)}{dM} b(M,z) \int dz_{st} y_l(M,z, z_{st}) \right]^2 P_{lin} \left(\frac{l}{\chi(z)} \right), \quad (19)$$

where the halo mass function is computed at z_{st} and h_{ν} is the spectral shape of non-thermal SZ distortion and is different from g_{ν} for clusters. For $M = 10^{12} M_{\odot}$, $Q_J = 10^{46} \text{ ergs}^{-1}$ and $t_J = 10^7 \text{ yr}$, a jet starting at $z = 1$ expands to 1 Mpc by $z = 0.9$. For $t_J = 10^8 \text{ yr}$, it reaches the same scale by $z = 0.98$. For higher luminosity $Q_J = 10^{47} \text{ ergs}^{-1}$ and $t_J \gtrsim 10^7 \text{ yr}$, it takes $\Delta z < 0.01$ to reach 1 Mpc. The characteristic size, chosen to be $\sim \text{Mpc}$ roughly decides the shape of the power spectrum.

In Fig. 8, we compare the one-halo contribution to the SZ power spectrum from radio galaxies to that from clusters at 150 GHz. At this frequency, g_{ν} of thermal y -distortion = -0.95 ; however, the non-thermal spectrum h_{ν} depends on the electron spectrum. We use h_{ν} from the non-thermal electron distribution for two different spectral index, $\alpha_p = (2.3, 3)$ as shown in the figure. As seen in the figure, for luminosities in the range $10^{45} - 10^{47} \text{ ergs}^{-1}$, the 1-halo contribution from radio galaxies is at least an order of magnitude smaller than from galaxy clusters. Higher jet lifetime and a steeper electron spectrum gives greater contribution to C_{ℓ}^{NT} . Since smaller jet lifetimes leads to cocoons of smaller sizes, the peak of the power spectrum moves to higher ℓ values. For $t_J = 10^8 \text{ yr}$, the power spectrum peaks at $\ell = 3000$ or $\theta \sim 2\text{-}3 \text{ arc minutes}$ which can be resolved by CMB experiments such as Atacama Cosmology Telescope (ACT)(Madhavacheril et. al. 2020) or South Pole Telescope (SPT)(Reichardt et. al. 2021) with angular resolution of 1.5 and 1 arcminute respectively. We also compare the two-halo terms and see similar pattern as in one-halo term except that the location of peaks of C_{ℓ}^{NT} curves are less visibly sensitive to change in parameters. The total power spectrum (i.e the sum of both 1-halo and 2-halo terms) is shown in Fig. 9, where we only consider one population of non-thermal electrons with $\alpha_p = 3$. It is seen that the total $C_{\ell}^{NT} \sim 1\%$ of the thermal SZ C_{ℓ} from clusters for most of the ℓ -range. C_{ℓ}^{NT} , quite obviously, depends on both cosmology and radio galaxy physics. For example, for $\ell \gtrsim 2000$, the $C_{\ell}^{NT} \propto \sigma_8^{4\text{-}4.5}$. For the most sensitive radio galaxy parameter α_M , the $C_{\ell}^{NT} \propto \alpha_M^{4.5}$ at its peak, but falls to $C_{\ell}^{NT} \propto \alpha_M^3$ by $\ell \sim 10^4$.

Given the emergence of precision cosmology, it is important for future, higher resolution, CMB experiments to take into account the contribution/contamination from radio galaxy cocoons when constraining cosmology and cluster physics using cluster SZ C_{ℓ} .

Till now, we have mainly considered current surveys like ACT and SPT, and the future survey proposal PIXIE. However, the other future high angular resolution and multi-frequency experiments, funded or proposed, are ready to explore the rich landscape of secondary CMB anisotropies. In particular, the CMB-S4 effort² and newly proposed CMB-HD³ are extremely promising for exploring the CMB distortions discussed in this paper. Keeping this in mind, we also look at the prospects of exploring the ntSZ from radio galaxy lobes with a CMB-HD like experiments in the next sections.

² <https://cmb-s4.org/>

³ <https://cmb-hd.org/>

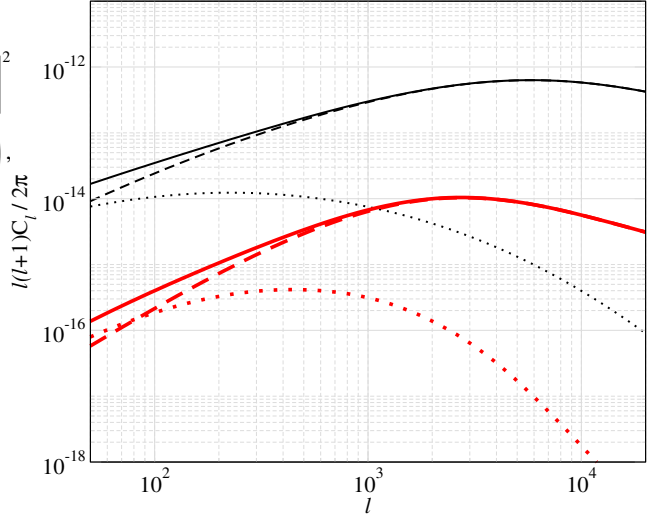


Figure 9. Comparison of one-halo (dashed lines), two-halo (dotted lines) and total (solid lines) SZ power spectrum contribution from radio galaxies (thick red lines) and galaxy clusters (thin black lines) at 150 GHz. Here, $Q_J = 10^{45} - 10^{47} \text{ ergs}^{-1}$, $t_J = 10^8 \text{ yr}$, $\alpha_p = 3$.

7 PROSPECTS FOR MULTI-FREQUENCY DETECTION OF ntSZ FLUCTUATIONS

In this section, we look at the prospect of detecting the cosmological ntSZ fluctuation power spectrum using multifrequency subtraction of thermal SZ power spectrum from galaxy clusters and other astrophysical foregrounds using the Internal Linear Combination (ILC) method (Tegmark et al. 2000). The central idea is to find a linear combination of frequency maps that minimize the variance of our desired signal. As an example, we consider the case when we want to extract tSZ signal from multifrequency CMB maps ignoring ntSZ from radio galaxies for the moment. We start by writing

$$\hat{a}_{lm}^{SZ} = \sum_{\nu} \frac{w_{\nu} a_{lm}(\nu)}{g_{\nu}}, \quad (20)$$

where a_{lm}^{SZ} is our estimator for tSZ signal in Rayleigh-jeans limit (where $g_{\nu} \rightarrow 1$), w_{ν} is the linear weight of each frequency map, g_{ν} is the tSZ spectral factor and $a_{lm}(\nu)$ is the spherical harmonic coefficients of total temperature anisotropies at frequency ν_i . The total signal a_{lm} is given by $a_{lm} = \sum_f a_{lm}^f + a_{lm}^{SZ}$, where f stands for foregrounds which are the other astrophysical and cosmological signal except the signal that we want to extract. We require that the variance $\langle \hat{a}^{SZ} \hat{a}^{SZ} \rangle$ is minimized subject to $\sum w_{\nu} = 1$. The expression of w_{ν} is then given by,

$$w_{\nu} = \frac{C_{ij}^{-1} e_j}{e_k C_{kl}^{-1} e_l}, \quad (21)$$

where $C_{ij} = \sum_f \frac{C^f(\nu_i, \nu_j)}{g_{\nu_i} g_{\nu_j}}$ is the correlation matrix of foregrounds (i.e. all signals except tSZ in this example) across frequency ν_i and ν_j and e_j is a one-dimensional matrix with all entries as 1. If foregrounds (i.e. C_{ij}^f) dominate at a particular frequency channel, then the above procedure simply puts a lower weight to that frequency channel to minimize the contribution from the foreground.

In addition to the foregrounds, we also need to consider the instrumental noise, which after multifrequency subtraction is given by, $N_l = w_{\nu} C_{ij} w_{\nu}$. After averaging over 'm's for each multi-

pole l , and for a sky fraction ($f_{\text{sky}} = 0.7$), the noise is given by $N_l / \sqrt{f_{\text{sky}}(2\ell + 1)}$. Similar to the noise, the contamination from each foreground can be obtained by replacing C_{ij} by C_{ij}^f in the above expression. The different foregrounds that we consider are those from free-free emission, synchrotron, dust and radio point sources and IR point sources. We use the expression of C_{ij}^f for these components from Tegmark et al. (2000); Hill & Pajer (2013). We list them in the appendix for completeness.

Our ultimate goal is to see if ntSZ signal from radio galaxies, which is roughly 1% of thermal SZ from galaxy clusters at $l \sim 1000$, can be detected in future. For this purpose, we consider an ambitious "PIXIE-like" experiment. Since PIXIE has 400 frequency bands (Kogut et al. 2011), the multifrequency subtraction will involve inverting a 400×400 matrix. For exploratory purpose, we consider a simpler exercise with 15 and 30 frequency bands which are logarithmically spaced between 30 GHz and 850 GHz. We assume that our hypothetical experiment has same noise budget as PIXIE. The sensitivity of PIXIE at each frequency band is $\Delta I = 4 \times 10^{-24} \text{ Wm}^{-2} \text{ sr}^{-1} \text{ Hz}^{-1}$ and the resolution is 2.6 degree which translates to $l = \pi/\theta \approx 70$, beyond which the instrumental noise increase exponentially as can be seen from Eq. A1. However, for our hypothetical experiment, we assume that the resolution is of the order of few arc minutes, such that the corresponding l is approximately $5 \times 10^3 - 10^4$. In Fig. 10, we plot the diagonal element of $C^f(v_i, v_j)$ s for each noise component in our experiment at $l = 2000$. Over here, the thermal SZ from galaxy clusters are an additional source of foreground (or noise) for the extraction of non-thermal SZ from radio galaxies.

The multifrequency subtraction procedure described here assumes each noise component to be uncorrelated with other. The thermal SZ from galaxy clusters and ntSZ from radio galaxies may be correlated with each other if they both reside in the same dark matter halos. However, we are interested in ntSZ from field radio galaxies and ignore such complications in this work. The thermal SZ signal is given by an analytical formula and, therefore, the correlation matrix for tSZ across frequency is perfectly correlated just like primary CMB. Next, we follow the same procedure as done before for extracting tSZ signal with Planck (Hill & Pajer 2013) and the result is shown in Fig. 11. As seen in the figure, we are able to significantly reduce the total noise (shown by dashed maroon) for 30 channels with our hypothetical experiment compared to Planck (dotted orange line). The reduction of noise allows us to come within a factor of 2-3 of detection threshold of non-thermal SZ at $l \sim 1000$. At l higher than the resolution of our experiment, instrumental noise dominate. The increase in number of frequency bands, from 15 to 30, does not lead to significant reduction of noise level; however, a much larger number of frequency bands may be able to make a difference. The reduction of overall noise in PIXIE is due to lower instrument noise. Once the noise due to foregrounds starts to dominate, any further reduction of instrumental noise does not make a difference. This is because the covariance matrix is dominated by few foreground components such as CMB, dust and IR at $l = 2000$ in Fig. 10 which then determines the weights that we obtain after variance minimization in Eq. 21. These weights may not be optimal for sub-dominant components such as radio point sources and tSZ. Therefore, even if we manage to remove the dominant components with more frequency bands, it does not necessarily make a significant change to cleaning of sub-dominant components. For a more optimized cleaning procedure, one may use constrained ILC (c-ILC) (Remazeilles et al. 2011) which puts additional constraints on the unwanted spectral components. Encouraged by the possibility of having S/N within a factor few with

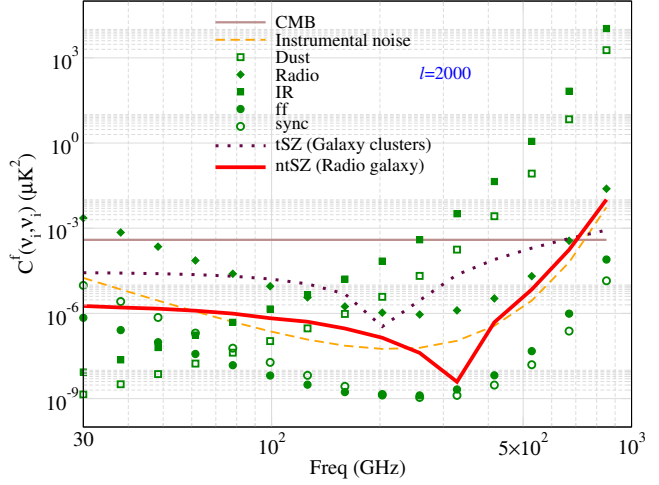


Figure 10. Diagonal elements of C_l^f as a function of frequency at $l = 2000$ for a PIXIE-like experiment. See the text for details.

our simplistic ILC method, we conclude that the detection of ntSZ may be within reach with a more optimized analysis for a futuristic PIXIE-like experiment.

We also do a quick estimate for the proposed CMB-HD survey (Sehgal et al. 2019), which has a lower noise level than PIXIE (see violet dot-dashed line in Fig 11) but with 7 frequency bands between 30-350 GHz. This frequency range may not be enough to distinguish ntSZ from thermal distortions (see Fig. 11 of Acharya et al. (2021) and related discussions) and a few additional high frequency channels ($\gtrsim 500$ GHz) may be needed to distinguish ntSZ clearly. Since the CMB-HD proposal is still in its beginning stage, for this work, we assume that there may be additional sufficient frequency coverage to distinguish various distortions. With CMB-HD, the noise becomes larger than the ntSZ only above $l \sim 7000$, and hence a strong detection of ntSZ becomes within reach.

8 IMPLICATIONS, DISCUSSIONS AND CONCLUSION

In this section, we do a fisher matrix estimate on how well we can constrain our radio galaxy physics, parameterized by $\{\alpha_p, t_J, \beta, A_{\text{HOD}}, \alpha_M\}$ if C_ℓ^{NT} can be extracted from observations. Note, that the C_ℓ^{NT} 's are also dependent on cosmological parameters on which strong priors already exist (Aghanim et al. 2020). These cosmological priors, along with other conservative priors on the radio galaxy parameters, can be used to break the strong parameter degeneracies. We list the most relevant cosmological parameters for the determination of C_ℓ^{NT} in Table 1. For the present work, we fix all the cosmological parameters to their mean values (except σ_8) since we expect these cosmological parameters to have a negligible effect on C_ℓ^{NT} given the precision of their measured values. However, we treat σ_8 which appears in the exponential in halo mass function as a free parameter and impose Planck prior.

In Fig. 12, we plot the multipole dependence of the fractional changes to C_ℓ^{NT} , to explore the impact on the C_ℓ^{NT} if we change the fiducial radio galaxy parameters and σ_8 . The fractional changes in C_ℓ^{NT} due to change in the fiducial α_p, A_{HOD} are independent of ℓ and hence degenerate. This is expected as changing α_p or A_{HOD} simply rescales the C_ℓ^{NT} . Changing σ_8 has almost ℓ independent behaviour. We have checked that the low- ℓ dependence is due to the choice of our high mass cutoff ($M = 10^{14} M_\odot$) of dark matter halos hosting

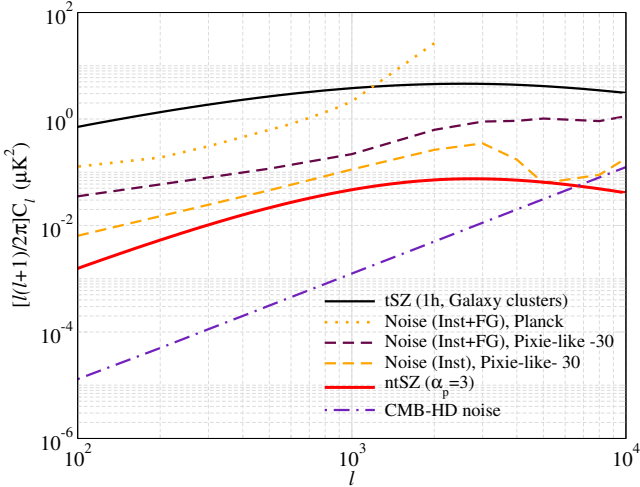


Figure 11. Instrumental (Inst) noise (dashed orange), instrumental+foreground (FG) noise (dashed maroon) after applying ILC to extract non-thermal SZ signal from radio galaxies with $Q_J = 10^{45} - 10^{47} \text{ ergs}^{-1}$, $t_J = 10^8 \text{ yr}$ and $\alpha_p = 3$ for a PIXIE-like experiment with 30 frequency channels having $\sim \text{arc-min}$ resolution ($\ell \sim 10^4$). We have added Planck noise in dotted orange and tSZ signal from galaxy clusters for reference. (see text for the description). We also show noise for the proposed CMB-HD experiment in dot-dashed violet line.

radio galaxies. However, the change to C_ℓ^{NT} due to jet lifetime has ℓ dependence at high- ℓ s. For low jet lifetimes, the jet shuts off before the radio galaxy expands to $\sim \text{Mpc}$ sizes at which point the pressure profile inside the lobe changes (Fig. 5) giving rise to the dependency on ℓ . The impact of β on fractional change in C_ℓ^{NT} also has ℓ dependence since a change in β changes the relative numbers of larger-to-smaller sized radio galaxy cocoons. Changing α_M boosts the relative jet luminosity in bigger halos, hence has some scale dependence. The dip in the curve for β is decided by the pivot point of HOD which is between $10^{12} - 10^{14} M_\odot$. Finally, in Fig. 13, we plot $\partial C_\ell^{NT} / \partial p_i$, i.e. the sensitivity of C_ℓ^{NT} on the parameters $\{p_i\}$ which enters the fisher matrix estimate using Eq. 12.

We work in the ideal scenario where the foregrounds are removed such that only the instrumental noise (shown in Fig. 11) remains and enters the error estimates. For the Fisher calculations, we bin the C_ℓ^{NT} in 50 logarithmically spaced ℓ bins between 100 to 10000. From Fig. 13, it can be seen that among the radio galaxy parameters, the C_ℓ^{NT} 's are most sensitive to A_{HOD} , α_M and the least sensitive to t_J . Given all other parameters fixed except a single parameter of interest, we can expect to determine $\{t_J, \alpha_p, \beta, A_{HOD}, \alpha_M\}$ at the level of $\{0.5, 4, 2, 41, 23\} \sigma$ s, respectively. For a CMB-HD like survey, the constraints strongly improve to $\{88, 583, 173, 6050, 4907\} \sigma$ s. However, when all parameters are free to vary, due to degeneracies between the different parameters, the constraints significantly weaken. Some of the degeneracies are broken by putting Planck prior on σ_8 , and further further observationally motivated (Smolčić et al. 2011) prior on A_{HOD} and β as $\sigma_{A_{HOD}}^{\text{Prior}} = 0.03$ and $\sigma_{\beta}^{\text{Prior}} = 0.3$.

In Tables 3 and 4, we list the constraints under the influence of different priors for a PIXIE and a CMB-HD like experiments. As expected, there is negligible improvement in the σ_8 constraint which is already available from Planck. The radio galaxy parameter constraints follow the trends already evident in Figure 13, with the mass scaling of the jet luminosity, α_M , being most tightly con-

strained. We find that, for PIXIE, α_M can be estimated at 4.7σ as soon as σ_8 prior is introduced. CMB-HD, with its higher sensitivity can constraint σ_8 to $\gtrsim 65\sigma$ even without σ_8 prior, which further increases to $\gtrsim 125\sigma$ when the σ_8 prior is added. It is interesting that A_{HOD} is not constrained with PIXIE even though the sensitivity of the C_ℓ^{NT} to A_{HOD} lies much above the noise in Figure 13. This can be understood from Fig 12 - change in the parameters that results in a near constant $\frac{\Delta C_\ell^{NT}}{C_\ell^{NT}}$ are strongly correlated, and hence A_{HOD} has strong degeneracies with both t_J & α_p . Moreover, A_{HOD} & β has direct correlation built in from the definition of $F(M)$. However, for CMB-HD, one can better the constrain on A_{HOD} to $\gtrsim 5\sigma$, a factor of two improvement over the prior on A_{HOD} . Note that α_p is expected to have values within 2.3 and 3 (Colafrancesco 2008; Colafrancesco & Marchegiani 2011). Imposing a theoretical prior based on equipartition of magnetic and particle energy densities, one can fix $\alpha_p = 3$. Whereas PIXIE can yield $\sigma_{\alpha_p} \sim 0.8$ and hence cannot differentiate between 2.3 and 3, a CMB-HD like experiment can achieve a factor of two better constraint and prefer one fiducial value of α_p over the other. PIXIE does a poor job on constraining β beyond its prior; however, CMB-HD can have $\gtrsim 5\sigma$ constraint of β , similar to A_{HOD} . Along with Q_J , the jet timescale t_J is one of the two main parameters affecting radio galaxy physics models. Due to the low signal to noise ratio for PIXIE, a fiducial $t_J = 10^8$ years can be constrained at $\sim 1.5\sigma$ (PIXIE) at best; however, CMB-HD has the potential to constrain $t_J > 8\sigma$. Within their own capabilities, both PIXIE and CMB-HD like experiments have the potential to improve our knowledge of radio galaxy physics and their relation to host halos at unprecedented levels.

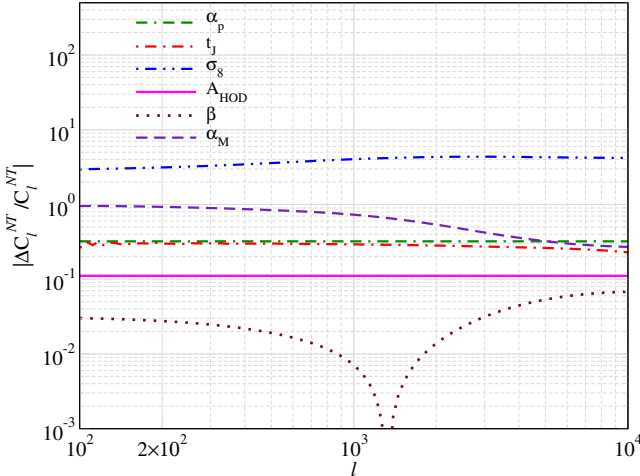
We have already seen above that, in the presence of Planck priors, the constraint on σ_8 from just using C_ℓ^{NT} is very weak. However, this additional source of SZ distortion can still be source of bias to σ_8 constraints using thermal SZ C_ℓ from galaxy clusters since at a particular frequency, say 150 GHz, the radio galaxy C_ℓ^{NT} can be a percent of cluster C_ℓ for $\ell > 1000$. We, of course, need to be careful to include the contribution from the spectral factor correctly. At 150GHz, g_ν for tSZ is -0.95 whereas h_ν for ntSZ is -0.4 (for $\alpha_p = 3$). Hence, the relative spectral boost of the tSZ compared to ntSZ is $0.95^2/0.4^2 = 5$. Since, the typical dependence of the SZ power spectrum on σ_8 goes approximately as $C_\ell \propto \sigma_8^{6-8}$, the impact of misattributing the ntSZ from radio galaxies to thermal SZ from clusters could bias σ_8 to percent level. Although this bias appears small, given that current constraints on σ_8 from both primary CMB (Aghanim et al. 2020) as well ground based SZ observations (Chaubal et. al. 2021) have reached sub-percent level accuracy, it is important to investigate the impact of radio galaxy ntSZ contamination in more detail taking into account the degeneracies between cosmology and the radio galaxy model parameters.

In this work, we have considered the ntSZ from radio galaxies and have not focused on any additional distortion due to kinematic SZ (kSZ) from the bulk motion of the radio galaxies. The kSZ power spectrum depends upon the product of electron number density and velocity. For a radio lobe, as the lobe expands, the motion of electrons coming towards us and going away from us cancel each other out and only the bulk motion of radio galaxy matters. Assuming equipartition of energy inside the radio lobes, the number density of electrons inside the lobe is proportional to $p_c/m_e c^2$ (Kaiser et al. 1997), where p_c is the pressure inside the lobe. Therefore, the expression for kSZ power spectrum for radio lobes is equivalent to tSZ power spectrum modulated by v_{rms}^2 . Since, $\frac{v_{rms}}{c} \sim 10^{-3} - 10^{-4}$ over the redshift range under consideration, the

Parameters	Fiducial value	Priors	with σ_8 prior	with $\{A_{\text{HOD}}, \beta\}$ priors	with $\{\sigma_8, A_{\text{HOD}}, \beta\}$ priors	with α_p fixed & $\{\sigma_8, A_{\text{HOD}}, \beta\}$ priors
α_M	1.0	-	0.215	0.645	0.215	0.215
α_p	3.0	-	no constraint	11.4	0.8	-
t_J (yrs)	10^8	-	1.36×10^8	1.23×10^8	0.72×10^8	0.68×10^8
β	0.86	0.3	3.5	0.29	0.29	0.29
A_{HOD}	0.09	0.03	no constraint	0.03	0.03	0.027
σ_8	0.8102	0.006	0.006	0.0059	0.0059	0.0059

Table 3. PIXIE like experiment forecast: 1- σ uncertainty on σ_8 and radio galaxy parameters for different priors.

Parameters	Fiducial value	Priors	with σ_8 prior	with $\{A_{\text{HOD}}, \beta\}$ priors	with $\{\sigma_8, A_{\text{HOD}}, \beta\}$ priors	with α_p fixed & $\{\sigma_8, A_{\text{HOD}}, \beta\}$ priors
α_M	1.0	-	0.008	0.015	0.007	0.007
α_p	3.0	-	no constraint	0.57	0.37	-
t_J (yrs)	10^8	-	1.35×10^7	1.23×10^7	1.23×10^7	1.06×10^7
β	0.86	0.3	0.15	0.17	0.13	0.13
A_{HOD}	0.09	0.03	no constraint	0.03	0.03	0.016
σ_8	0.8102	0.006	0.006	0.042	0.0059	0.0059

Table 4. CMB-HD like experiment forecast: 1- σ uncertainty on σ_8 and radio galaxy parameters for different priors.**Figure 12.** Fractional change in the one halo C_ℓ^{NT} of radio galaxies due to change in radio galaxy parameters and σ_8 by 10 percent. The fiducial parameters are $\alpha_p = 3$, $t_J = 10^7$ yr, $\sigma_8 = 0.81$, $\beta = 0.86$, $A_{\text{HOD}} = 0.09$ and $\alpha_M = 1$.

kSZ power spectrum is 6-8 orders of magnitude smaller than the ntSZ power spectrum and can be ignored.

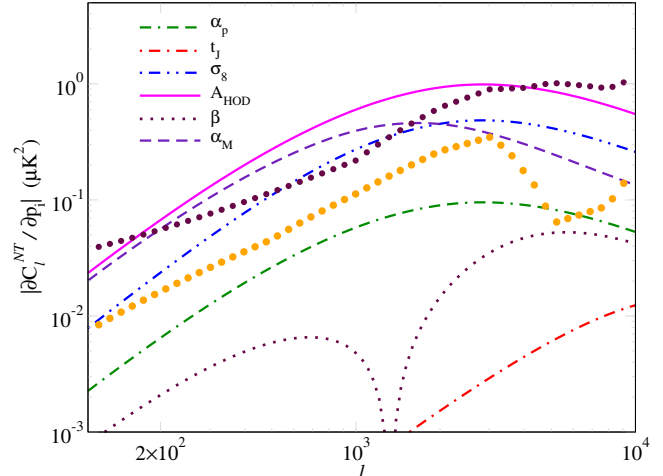
Given the rewards, we hope that the search and detection of non-thermal SZ from radio galaxies be one of the key goals of all future CMB observation missions envisioned, like CMB-S4 (Abazajian et al. 2016), CMB-HD, and others.

ACKNOWLEDGEMENTS

The authors would like to thank Jens Chluba and Rishi Khatri for discussions. SKA is supported by the ERC Consolidator Grant *CMBSPEC* (No. 725456). SM acknowledges support of the Department of Atomic Energy, Government of India, under project no. 12-R&D-TFR-5.02-0200.

9 DATA AVAILABILITY

The data underlying in this article are available in this article.

**Figure 13.** $\frac{\partial C_\ell^{NT}}{\partial p_i}$ where p_i s are the parameters as denoted in the plot. For t_J , the unit of time is per 10^7 yr. We also show the instrumental noise (orange circles) and total noise (maroon circles) for a PIXIE-like experiment in Fig. 11.

REFERENCES

Abazajian et. al. K. N., 2016, arXiv e-prints, arXiv:1610.02743
 Abitbol M. H., Chluba J., Hill J. C., Johnson B. R., 2017, MNRAS, 471, 1126
 Acharya S. K., Majumdar S., Nath B. B., 2021, MNRAS, 503, 5473
 Ade et. al. P. A. R., 2021, Phys.Rev.Lett, 127, 151301
 Aghanim N., Desert F. X., Puget J. L., Gispert R., 1996, A&A, 311, 1
 Aghanim N., Majumdar S., Silk J., 2008, Reports on Progress in Physics, 71, 066902
 Aghanim N., et al., 2020, A&A, 641, A6
 Alexander P., Leahy J. P., 1987, MNRAS, 225, 1
 Arnaud M., Pratt G. W., Piffaretti R., Böhringer H., Croston J. H., Pointecouteau E., 2010, A&A, 517, A92
 Begelman M. C., Cioffi D. F., 1989, ApJL, 345, L21
 Berlind A. A. et al., 2003, ApJ, 593, 1
 Birkinshaw M., 1999, Phys. Rep., 310, 97
 Blas D., Lesgourgues J., Tram T., 2011, JCAP, 2011, 034
 Bolliet B., Comis B., Komatsu E., Macías-Pérez J. F., 2018, MNRAS, 477, 4957
 Challinor A., Lasenby A., 1998, ApJ, 499, 1

Chaubal et. al. P. S., 2021, arXiv e-prints, arXiv:2111.07491

Chluba J., 2016, MNRAS, 460, 227

Chluba J., Khatri R., Sunyaev R. A., 2012, MNRAS, 425, 1129

Chluba J., Sunyaev R. A., 2012, MNRAS, 419, 1294

Chluba et. al. J., 2021, Experimental Astronomy, 51, 1515

Colafrancesco S., 2008, MNRAS, 385, 2041

Colafrancesco S., Marchegiani P., 2011, A&A, 535, A108

Cooray A., Sheth R., 2002, Phys. Rep., 372, 1

Croston J. H., Hardcastle M. J., Harris D. E., Belsole E., Birkshaw M., Worrall D. M., 2005, ApJ, 626, 733

Dolgov A. D., Hansen S. H., Pastor S., Semikoz D. V., 2001, ApJ, 554, 74

Dubrovich V. K., 1975, Soviet Astronomy Letters, 1, 196

Duffy A. R., Schaye J., Kay S. T., Dalla Vecchia C., 2008, MNRAS, 390, L64

Dvorkin C., Hu W., Smith K. M., 2009, Phys. Rev. D, 79, 107302

Enßlin T. A., Kaiser C. R., 2000, A&A, 360, 417

Erlund M. C., Fabian A. C., Blundell K. M., 2008, MNRAS, 386, 1774

Fabian A. C., Chapman S., Casey C. M., Bauer F., Blundell K. M., 2009, MNRAS, 395, L67

Felten J. E., Rees M. J., 1969, Nature, 221, 924

Fixsen et. al D. J., 1996, ApJ, 473, 576

Fukazawa Y., Makishima K., Ohashi T., 2004, PASJ, 56, 965

Hardcastle M. J., Croston J. H., 2020, arXiv e-prints, arXiv:2003.06137

Hart L., Rotti A., Chluba J., 2020, MNRAS, 497, 4535

Hill J. C., Battaglia N., Chluba J., Ferraro S., Schaan E., Spergel D. N., 2015, Phys. Rev. Lett., 115, 261301

Hill J. C., Pajer E., 2013, Phys. Rev. D, 88, 063526

Holder G., Chluba J., 2021, arXiv e-prints, arXiv:2110.08373

Hu W., 2000, ApJ, 529, 12

Hu W., Kravtsov A. V., 2003, ApJ, 584, 702

Hu W., Scott D., Silk J., 1994, ApJL, 430, L5

Hu W., White M., 1997, New Astron., 2, 323

Iqbal A., Kale R., Nath B. B., Majumdar S., 2018, MNRAS, 480, L68

Isobe N., Koyama S., 2015, PASJ, 67, 77

Isobe N., Tashiro M. S., Gandhi P., Hayato A., Nagai H., Hada K., Seta H., Matsuta K., 2009, ApJ, 706, 454

Itoh N., Kohyama Y., Nozawa S., 1998, ApJ, 502, 7

Jetha N. N., Ponman T. J., Hardcastle M. J., Croston J. H., 2007, MNRAS, 376, 193

Johnson O., Almaini O., Best P. N., Dunlop J., 2007, MNRAS, 376, 151

Kaiser C. R., Alexander P., 1997, MNRAS, 286, 215

Kaiser C. R., Dennett-Thorpe J., Alexander P., 1997, MNRAS, 292, 723

Kamionkowski M., Kosowsky A., Stebbins A., 1997, Phys. Rev. Lett., 78, 2058

Kauffmann G., Colberg J. M., Diaferio A., White S. D. M., 1999, MNRAS, 303, 188

Khatri R., Sunyaev R. A., 2012, JCAP, 2012, 038

Khatri R., Sunyaev R. A., Chluba J., 2012, A&A, 543, A136

Kogut et. al A., 2011, JCAP, 2011, 025

Komatsu E., Kitayama T., 1999, ApJL, 526, L1

Komatsu E., Seljak U., 2002, MNRAS, 336, 1256

Konar C., Hardcastle M. J., Jamrozy M., Croston J. H., 2013, MNRAS, 430, 2137

Leahy J. P., Williams A. G., 1984, MNRAS, 210, 929

Lee E., Chluba J., Holder G. P., 2021, arXiv e-prints, arXiv:2112.10666

Lewis A., Challinor A., 2006, Phys. Rep., 429, 1

Ma C.-P., Fry J. N., 2002, Phys. Rev. Lett., 88, 211301

Madhavacheril et. al. M. S., 2020, Phys. Rev. D, 102, 023534

Majumdar S., 2001a, PhD thesis (Indian Institute of Science, Bangalore)

Majumdar S., 2001b, ApJL, 555, L7

Majumdar S., Nath B. B., Chiba M., 2001, Monthly Notices of the Royal Astronomical Society, 324, 537

Majumdar S., Subrahmanyan R., 2000, MNRAS, 312, 724

Malu S., Datta A., Colafrancesco S., Marchegiani P., Subrahmanyan R., Narasimha D., Wieringa M. H., 2017, Scientific Reports, 7, 16918

Matsubara T., 2004, ApJ, 615, 573

McQuinn M., Furlanetto S. R., Hernquist L., Zahn O., Zaldarriaga M., 2005, ApJ, 630, 643

Molnar S. M., Birkshaw M., 2000, ApJ, 537, 542

Mukherjee S., Paul S., Choudhury T. R., 2019, MNRAS, 486, 2042

Natarajan A., Battaglia N., Trac H., Pen U. L., Loeb A., 2013, ApJ, 776, 82

Natarajan P., Sigurdsson S., 1999, MNRAS, 302, 288

Nath B. B., 1995, MNRAS, 274, 208

Nath B. B., 2010, MNRAS, 407, 1998

Nath B. B., Roychowdhury S., 2002, MNRAS, 333, 145

Omrao H., Binney J., 2004, MNRAS, 350, L13

Planck, 2013, A&A, 550, A131

Planck Collaboration, Aghanim et. al. N., 2016, A&A, 594, A22

Rees M. J., Sciama D. W., 1968, Nature, 217, 511

Reichardt et. al. C. L., 2021, ApJ, 908, 199

Remazeilles M., Boullet B., Rotti A., Chluba J., 2019, MNRAS, 483, 3459

Remazeilles M., Delabrouille J., Cardoso J.-F., 2011, MNRAS, 410, 2481

Reynolds C. S., Begelman M. C., 1997, ApJL, 487, L135

Roy A., Kulkarni G., Meerburg P. D., Challinor A., Baccigalupi C., Lapi A., Haehnelt M. G., 2021, JCAP, 2021, 003

Sachs R. K., Wolfe A. M., 1967, ApJ, 147, 73

Sarkar S., Cooper A. M., 1984, Physics Letters B, 148, 347

Sazonov S. Y., Sunyaev R. A., 1998, ApJ, 508, 1

Schaan et. al. E., Atacama Cosmology Telescope Collaboration, 2021, Phys. Rev. D, 103, 063513

Scheuer P. A. G., 1974, MNRAS, 166, 513

Sehgal et. al. N., 2019, in Bulletin of the American Astronomical Society, Vol. 51, p. 6

Shabala S. S., Ash S., Alexander P., Riley J. M., 2008, MNRAS, 388, 625

Shaw L. D., Rudd D. H., Nagai D., 2012, ApJ, 756, 15

Smolčić V., Finoguenov A., Zamorani G., Schinnerer E., Tanaka M., Giordini S., Scoville N., 2011, MNRAS, 416, L31

Sunyaev R. A., Chluba J., 2009, Astronomische Nachrichten, 330, 657

Sunyaev R. A., Zeldovich Y. B., 1970, ApSS, 7, 20

Sunyaev R. A., Zeldovich Y. B., 1980, MNRAS, 190, 413

Tegmark M., Eisenstein D. J., Hu W., de Oliveira-Costa A., 2000, ApJ, 530, 133

Tegmark M., Taylor A. N., Heavens A. F., 1997, ApJ, 480, 22

Tinker J., Kravtsov A. V., Klypin A., Abazajian K., Warren M., Yepes G., Gottlöber S., Holz D. E., 2008, ApJ, 688, 709

Tinker J. L., Robertson B. E., Kravtsov A. V., Klypin A., Warren M. S., Yepes G., Gottlöber S., 2010, ApJ, 724, 878

Tucker W., David L. P., 1997, ApJ, 484, 602

Wake D. A., Croom S. M., Sadler E. M., Johnston H. M., 2008, MNRAS, 391, 1674

Yamada M., Sugiyama N., Silk J., 1999, ApJ, 522, 66

Zaldarriaga M., Seljak U., 1997, Phys. Rev. D, 55, 1830

Zeldovich Y. B., Sunyaev R. A., 1969, ApSS, 4, 301

APPENDIX A: FOREGROUNDS AND INSTRUMENTAL NOISE

The following expression for noise and foregrounds have been used [Hill & Pajer \(2013\)](#). The experimental noise is given by,

$$C_l^N(\nu, \nu') = \delta_{\nu, \nu'} \Delta T(\nu)^2 e^{l(l+1)\theta(\nu)^2} (8\ln 2) \theta(\nu)^2 \quad (A1)$$

The value of $\Delta T(\nu)$ and $\theta(\nu)$ for Planck experiment can be found in Table 1 of [Hill & Pajer \(2013\)](#). For the cosmological foregrounds, we parameterize C^f as,

$$C^f(\nu_i, \nu_j) = \frac{\Theta^f(\nu_i)\Theta^f(\nu_j)}{\Theta^f(\nu_0)^2} R(\nu_i, \nu_j) C_\ell, \quad (A2)$$

where $\Theta(\nu)$ is the frequency spectrum of a particular foreground and $R(\nu_i, \nu_j)$ is the correlation factor across the frequency whose expression is $R(\nu_i, \nu_j, \alpha) = \exp\left[-\frac{1}{2}(\log(\nu_i/\nu_j)/\zeta^f)^2\right]$ with $\zeta^f = (\sqrt{2}\alpha)^{-1}$. The instrumental noise is perfectly uncorrelated across frequency while the CMB is perfectly correlated. Other cosmological foregrounds lie in between.

The frequency distribution is given by,

$$\Theta^{CMB}(\nu) = 1. \quad (\text{A3})$$

$$\Theta^{ff}(\nu) = \nu^{-2.15} c(\nu) \quad (\text{A4})$$

$$\Theta^{Dust}(\nu) = \frac{c(\nu)c(\tilde{\nu})\nu^{4.7}}{e^{\frac{\nu}{56.8}\frac{2.725}{18}} - 1} \quad (\text{A5})$$

$$\Theta^{sync}(\nu) = \nu^{-2.8} c(\nu) \quad (\text{A6})$$

$$\Theta^{radio}(\nu) = \nu^{-0.5} \left[\frac{\partial I(\nu, T)}{\partial T} \right]_{T_{CMB}}^{-1} \quad (\text{A7})$$

$$\Theta^{IR}(\nu) = \nu^{2.1} I(\nu, 9.7\text{K}) \left[\frac{\partial I(\nu, T)}{\partial T} \right]_{T_{CMB}}^{-1} \quad (\text{A8})$$

with $c(\nu) = \left[\frac{2\sinh(x/2)}{x} \right]^2$, where $x = \frac{h\nu}{kT_{CMB}}$ and $c(\tilde{\nu}) \propto \nu^{-2}$.

The expression for C^f is then given by,

$$C_l^{CMB}(\nu_i, \nu_j) = C_l^{CMB} \quad (\text{A9})$$

$$C_l^{ff}(\nu_i, \nu_j) = \frac{\Theta^{ff}(\nu_i)\Theta^{ff}(\nu_j)}{\Theta^{ff}(31\text{GHz})^2} (70\mu\text{K})^2 \ell^{-3} R(\nu_i, \nu_j, 0.02) \quad (\text{A10})$$

$$C_l^{Dust}(\nu_i, \nu_j) = \frac{\Theta^{Dust}(\nu_i)\Theta^{Dust}(\nu_j)}{\Theta^{Dust}(90\text{GHz})^2} (24\mu\text{K})^2 \ell^{-3} R(\nu_i, \nu_j, 0.3) \quad (\text{A11})$$

$$C_l^{sync}(\nu_i, \nu_j) = \frac{\Theta^{sync}(\nu_i)\Theta^{sync}(\nu_j)}{\Theta^{sync}(19\text{GHz})^2} (101\mu\text{K})^2 \ell^{-2.4} R(\nu_i, \nu_j, 0.15) \quad (\text{A12})$$

$$C_l^{radio}(\nu_i, \nu_j) = \frac{\Theta^{radio}(\nu_i)\Theta^{radio}(\nu_j)}{\Theta^{radio}(150\text{GHz})^2} (\sqrt{3}\mu\text{K})^2 \frac{2\pi}{\ell(\ell+1)} \left[\frac{\ell}{3000} \right]^2 R(\nu_i, \nu_j, 0.5) \quad (\text{A13})$$

$$C_l^{IR}(\nu_i, \nu_j) = \frac{\Theta^{IR}(\nu_i)\Theta^{IR}(\nu_j)}{\Theta^{IR}(150\text{GHz})^2} \frac{2\pi}{\ell(\ell+1)} (7\mu\text{K}^2 \left(\frac{\ell}{3000} \right)^2 + 5.7\mu\text{K}^2 \left(\frac{\ell}{3000} \right)^{0.8}) R(\nu_i, \nu_j, 0.3) \quad (\text{A14})$$

We first try to extract tSZ signal from galaxy clusters, ignoring ntSZ from radio galaxies. This exercise was done in Hill & Pajer (2013). We repeat the exercise as a check of our calculations. We begin by using the procedure described in Sec. 7 to look at the prospect of detecting thermal SZ signal in Planck which has 9 frequency channels. In Fig. A1 and A2, we plot the frequency dependence of $C^f(\nu_i, \nu_i)$ for two multipoles, $\ell = 100, 1000$, using Planck instrumental noise. The dominant foregrounds are dust, IR point sources and instrumental noise at high frequencies and CMB at intermediate frequencies. At high multipoles (like $\ell = 1000$), the instrumental noise also dominates at all frequencies.

Given the frequency dependence of the foregrounds as shown in Fig. A1 and A2, we show the possibility of extracting the thermal SZ signal with Planck sensitivity and frequency bands in Fig. A3. The instrumental noise is perfectly decorrelated across frequencies and, therefore, it dominates the total noise budget. The

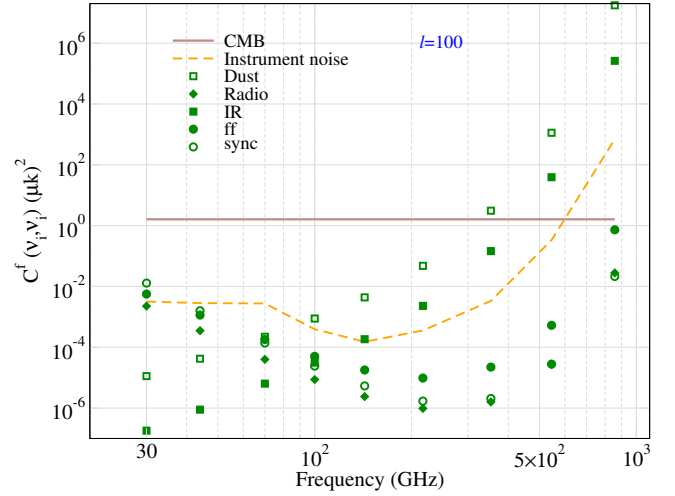


Figure A1. Diagonal element of $C^f(\nu_i, \nu_i)$ for each foreground for tSZ extraction (ignoring ntSZ) as a function of frequency at $\ell = 100$.

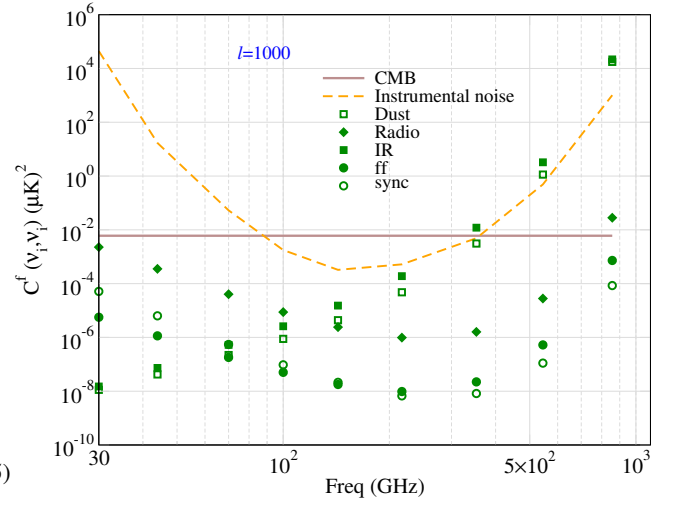


Figure A2. Same as Fig A1 but at $\ell = 1000$.

residual CMB and the other dominant foregrounds are well below the instrumental noise as the ILC procedure is efficient in cleaning correlated noise. The thermal SZ signal is well above the noise up to $\ell \sim 1000$. While this exercise was done with only 9 frequencies, more number of frequency channels will further reduce the residual foreground noise.

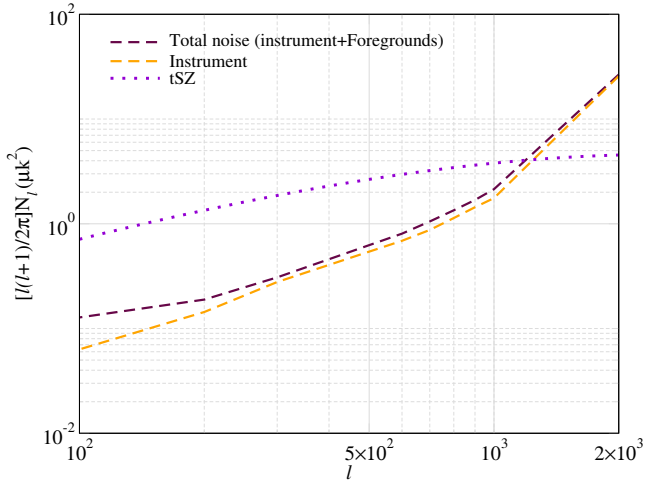


Figure A3. Noise after SZ signal extraction and comparison with the tSZ signal from Planck.